Engineering Conferences International
ECI Digital Archives

Sixth International Conference on Porous Media and Its Applications in Science, Engineering and Industry

Proceedings

7-6-2016

Modeling flow, heat and mass transfer in a porous biomass plug - when used in an electrically heated tobacco system

Markus Nordlund
Philip Morris Products S.A., markus.nordlund@pmi.com

Arkadiusz K. Kuczaj
Philip Morris Products S.A.

MODELING FLOW, HEAT AND MASS TRANSFER IN A POROUS BIOMASS PLUG – WHEN USED IN AN ELECTRICALLY HEATED TOBACCO SYSTEM

M. Nordlund[*1] and **A.K. Kuczaj**[1,2]

[1] *Philip Morris International Research & Development, Philip Morris Products S.A., Quai Jeanrenaud 5, CH-2000 Neuchâtel, Switzerland*

[2] *Multiscale Modeling & Simulation, Dept. of Applied Mathematics, University of Twente, P.O. Box 217, 7500 AE Enschede, The Netherlands.*

ABSTRACT

Heating porous biomass samples is utilized in many industries for drying or extracting Volatile Organic Compounds (VOC) from the biomass. The heating may trigger physical and chemical processes within the material, such as release of VOC, thermal degradation and evaporation. For most practical applications, it is important to have control of the complex processes occurring during heating to generate stable and controllable release of VOC. This is the case of an Electrically Heated Tobacco System (EHTS) delivering the released VOC to consumers by inhalation. In this work, Computational Fluid Dynamics (CFD) was used to model the physical and chemical processes numerically to demonstrate the operating conditions that the tobacco plug was exposed to during product use and to highlight the product functioning upon heating. The simulated temperature in the porous biomass plug was compared to experimental data obtained by thermocouples inserted into the biomass plug. In addition, the simulated amount of VOC exiting the product was compared to experimentally measured data for glycerol and nicotine. The close match between numerical and experimental results indicate that most relevant physical and chemical processes are understood and were accounted for in the numerical model. The tobacco plug was also shown to remain below the temperature controlled heater temperature during use.

Keywords: Heat and mass transfer, biomass, Electrically Heated Tobacco System

1 INTRODUCTION

Philip Morris International (PMI) is developing a range of novel tobacco products with the potential to reduce individual risk and population harm in comparison to smoking cigarettes. One of these products is the Tobacco Heating System 2.2 (THS 2.2), (named as the EHTS in this paper), already commercialized in a number of countries (e.g., Japan, Italy, Switzerland, Russia, Portugal and Romania). The two main components of the patented EHTS considered in this work are the specifically designed tobacco product (Electrically Heated Tobacco Product (EHTP)) containing the biomass plug and the Holder (heating device) into which the EHTP is inserted and which heats, rather than burns, the porous biomass plug by means of an electrically controlled heater. The heating triggers release of VOC from the biomass plug (containing processed tobacco sheets made from tobacco powder), locally increasing the density of the gas in the surrounding pore space. Air at ambient temperature is periodically drawn through the heated EHTP following a puffing protocol, transporting the released VOC through the EHTP, as shown in Figure 1. This results in both thermal and chemical nonequilibrium conditions with interstitial energy and mass transfer occurring between the gas and solid phases. Moreover, when cooled down, the VOC can reach supersaturation, resulting in aerosol droplet formation.

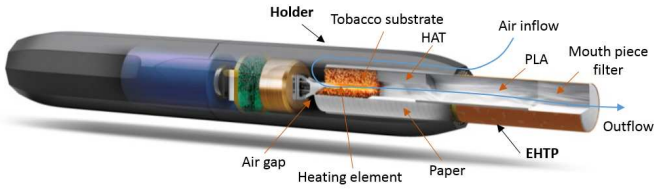

Figure 1: Flow path through the Holder and the EHTP containing a porous tobacco plug of the considered EHTS.

In this work we present our approach to model transient and density varying flow, heat and mass transfer in an EHTP containing an anisotropic porous biomass plug made from tobacco powder formed into sheets. To account for all these phenomena, volume averaged transient and density varying mass, momentum and energy conservation equations for multicomponent aerosols in anisotropic porous media under thermal and chemical nonequilibrium were solved using a segregated collocated variable finite volume algorithm implemented into the Open source Field Operations And Manipulations (OpenFOAM®) software package. The aim of this work was to investigate the functioning of the EHTS in terms of

*markus.nordlund@pmi.com

the temperature distribution in the biomass plug as well as the delivery of chemical compounds from the biomass during use under realistic operating conditions.

The paper is organized as follows. First, an overview of the modeling approach is given in Section 2. Thereafter, the simulation cases and conditions are introduced in Section 3.2, followed by descriptions of the validation experiments in Section 4. The results of the simulation are presented and discussed in Section 5. Finally, the outcome of the work is concluded in Section 6.

2 MODELING OF THE FUNCTIONING OF AN EHTS

2.1 Volume-averaged governing equations

Following the derivations in [1] and the closure modeling in [2], the volume-averaged mass, momentum and energy conservation equations for fluid flow, heat and mass transfer in anisotropic, heterogeneous porous media, constituted of a fluid phase α and a solid phase β, can in its closed general conservation form, assuming local thermal non-equilibrium between the phases, be written as:

$$\partial_t(\phi\langle\rho_\alpha\rangle^\alpha) + \partial_i(\langle\rho_\alpha\rangle^\alpha\langle u_i\rangle) + \hat{\Omega}_m = \phi\langle S_m^{\beta\to\alpha}\rangle^\alpha \tag{1}$$

$$\begin{aligned}\partial_t(\langle\rho_\alpha\rangle^\alpha\langle u_i\rangle) + \partial_j(\phi^{-1}\langle\rho_\alpha\rangle^\alpha\langle u_j\rangle\langle u_i\rangle) = \\ -\phi\partial_i\langle p_\alpha\rangle^\alpha + \partial_j\langle\tau_{ij}\rangle + \phi\langle\zeta_i\rangle^\alpha - \phi D_{ij}\langle u_j\rangle\end{aligned} \tag{2}$$

$$\begin{aligned}\langle c_{p,\alpha}\rangle^\alpha\langle\rho_\alpha\rangle^\alpha(\partial_t(\phi\langle T_\alpha\rangle^\alpha) + \langle u_i\rangle\partial_i\langle T_\alpha\rangle^\alpha) + \hat{\Lambda}_\alpha = \\ \partial_i(\lambda_{ij}^{\alpha\alpha}\partial_i\langle T_\alpha\rangle^\alpha) + \partial_i(\lambda_{ij}^{\alpha\beta}\partial_i\langle T_\beta\rangle^\beta) + \partial_t(\phi\langle p_\alpha\rangle^\alpha) + \\ \langle u_i\rangle\partial_i\langle p_\alpha\rangle^\alpha + h_{\alpha\beta}s_{\alpha\beta}(\langle T_\beta\rangle^\beta - \langle T_\alpha\rangle^\alpha) + \langle S_{e,\alpha}\rangle\end{aligned} \tag{3}$$

$$\begin{aligned}\langle c_{p,\beta}\rangle^\beta\langle\rho_\beta\rangle^\beta\partial_t((1-\phi)\langle T_\beta\rangle^\beta) = \partial_i(\lambda_{ij}^{\beta\beta}\partial_i\langle T_\beta\rangle^\beta) \\ +\partial_i(\lambda_{ij}^{\beta\alpha}\partial_i\langle T_\alpha\rangle^\alpha) - h_{\alpha\beta}s_{\alpha\beta}(\langle T_\beta\rangle^\beta - \langle T_\alpha\rangle^\alpha) + \langle S_{e,\beta}\rangle\end{aligned} \tag{4}$$

where t is the time, ρ the density, u_i the velocity in the x_i direction, $\hat{\Omega}_m$ is the mass dispersion, and $S_m^{\beta\to\alpha}$ is a mass source due to release of VOC. The extrinsic, or superficial, average of a property φ_α is denoted by $\langle\varphi_\alpha\rangle$ and the intrinsic volume average of phase α by $\langle\varphi_\alpha\rangle^\alpha = \phi\langle\varphi_\alpha\rangle$, where ϕ is porosity of the porous medium. The operator ∂_t is the temporal partial derivative and ∂_i is the partial derivative with respect to the spatial coordinate x_i. The pressure is denoted p, ζ_i a momentum body source including also higher-order perturbation terms originating from the volume averaging procedure and $\langle\tau_{ij}\rangle$ is the volume-averaged rate of strain tensor. $D_{ij} = \langle\mu\rangle^\alpha(K_{ij}^{-1} + K_{il}^{-1}F_{lj})$ is the anisotropic resistivity tensor, where K_{ij}^{-1} is the inverse of the permeability tensor and $F_{lj} = \frac{\langle\rho_\alpha\rangle^\alpha}{\langle\mu_\alpha\rangle^\alpha}K_{lj}^{1/2}|\langle u_i\rangle|c_E$ is the non-Darcy resistivity tensor, where c_E is the form drag coefficient and $\langle\mu_\alpha\rangle^\alpha$ is the dynamic viscosity.

In the energy equations, $c_{p,m}$ is the specific heat at constant pressure, λ_m is the thermal conductivity, and T_m the temperature for the phase $m \in \{\alpha, \beta\}$. Thermal dispersion is denoted $\hat{\Lambda}_\alpha$ and the effective conductivity tensors by $\lambda_{ij}^{\alpha\alpha}$, $\lambda_{ij}^{\alpha\beta}$, $\lambda_{ij}^{\beta\beta}$, and $\lambda_{ij}^{\beta\alpha}$. The effective thermal conductivity tensors are determined by the closure modeling by [3], and can be shown to depend on the effective thermal conductivity tensor at thermal equilibrium, λ_{ij}^e. The interfacial heat transfer coefficient is denoted by $h_{\alpha\beta}$ and $s_{\alpha\beta}$ is the specific surface area. $S_{e,\alpha}$ and $S_{e,\beta}$ are energy source terms related to release and phase changes. In Eqs. (2) to (4) the closure terms suggested in [2] were adopted.

Note that the volume-averaged equations can be used in both the pure fluid and in the porous region. In the pure fluid region, $\phi = 1$, $D_{ij} = \lambda_{ij}^{\beta\beta} = \lambda_{ij}^{\alpha\beta} = \lambda_{ij}^{\beta\alpha} = 0$, $h_{\alpha\beta} = s_{\alpha\beta} = 0$ and $\lambda_{ij}^{\alpha\alpha} = \lambda_\alpha I_{ij}$, where I_{ij} is the identity tensor.

Pure solid regions of the EHTS, i.e., the Holder parts, were represented by separate computational meshes. In these solid regions, only the solid temperature equation (4) was solved with $\langle T_\beta\rangle^\beta = T_\beta$, $\phi = 0$, $\lambda_{ij}^{\alpha\alpha} = \lambda_{ij}^{\alpha\beta} = \lambda_{ij}^{\beta\alpha} = 0$, $\lambda_{ij}^{\beta\beta} = \lambda_\beta I_{ij}$, $\langle c_{p,\beta}\rangle^\beta = c_{p,\beta}$, $\langle\rho_\beta\rangle^\beta = \rho_\beta$, and $h_{\alpha\beta} = s_{\alpha\beta} = 0$. Each solid region was connected to its neighbor or the fluid-porous region by the interface conditions specified by [4].

In addition to the volume averaged governing equations for the mixture, the transport equations for the gas phase mass fraction (Y_k) and liquid (droplet) phase mass fraction (Z_k) of compound k and the droplet number concentration N are solved for. They can be written as:

$$\begin{aligned}\partial_t(\phi\langle\rho_\alpha\rangle^\alpha\langle Y_k\rangle^\alpha) + \partial_i(\langle\rho_\alpha\rangle^\alpha\langle u_i\rangle\langle Y_k\rangle^\alpha) + \hat{\Omega}_k^Y = \\ -\partial_j\langle j_{j,k}\rangle + \phi(\langle S_k^{Z\to Y}\rangle^\alpha + \langle S_k^{\beta\to\alpha}\rangle^\alpha) \;\; ; \;\; k = 1, ..., n\end{aligned} \tag{5}$$

$$\begin{aligned}\partial_t(\phi\langle\rho_\alpha\rangle^\alpha\langle Z_k\rangle^\alpha) + \partial_i(\langle\rho_\alpha\rangle^\alpha\langle u_i\rangle\langle Z_k\rangle^\alpha) + \hat{\Omega}_k^Z = \\ \phi(\langle S_k^{Y\to Z}\rangle^\alpha + \langle S_k^{\alpha\to\beta}\rangle^\alpha) \;\; ; \;\; k = 1, ..., n\end{aligned} \tag{6}$$

$$\partial_t(\phi\langle N\rangle^\alpha) + \partial_i(\langle u_i\rangle\langle N\rangle^\alpha) + \hat{\Omega}^N = \phi\langle S_N\rangle^\alpha \tag{7}$$

where $S_k^{Z\to Y}$ and $S_k^{Y\to Z}$ are mass source terms due to phase change for compound k, $S_k^{\alpha\to\beta}$ and $S_k^{\beta\to\alpha}$ are mass source terms due to release or deposition of VOC, and S_N the source term for aerosol droplet creation and evolution.

In this work, the dispersion terms $\hat{\Omega}_m = \hat{\Omega}_k^Y = \hat{\Omega}_k^Z = \hat{\Omega}^N = \hat{\Lambda}_\alpha \approx 0$. This assumption and mass conservation impose the following constraints on the

mass fractions ($\sum_{k=1}^{n}(\langle Y_k\rangle^\alpha + \langle Z_k\rangle^\alpha) = 1$), diffusion fluxes ($\sum_{k=1}^{n}(\partial_j\langle j_{j,k}\rangle) = 0$), and the mass source terms $\sum_{k=1}^{n}(\langle S_k^{Y\to Z}\rangle^\alpha + \langle S_k^{Z\to Y}\rangle^\alpha) = 0$ and $\sum_{k=1}^{n}(\langle S_k^{\alpha\to\beta}\rangle^\alpha + \langle S_k^{\beta\to\alpha}\rangle^\alpha) = \langle S_m^{\beta\to\alpha}\rangle^\alpha$.

The approach used to simulated conjugate fluid/porous/solid regions follows that presented by [4, 5], but was extended for anisotropic porous media, multicomponent aerosol mixtures, density varying flows, as well as release of VOC from the porous biomass plug. The fluid-porous interface treatment by [6] was combined with the extended Pressure-Implicit with Splitting of Operators (PISO) algorithm by [7].

2.2 Effective properties models

The EHTP contains porous media with different topology, dimensions and porosities. Two porous media models were used to represent the effective properties of the porous parts of the EHTP. The first, named Random Fibers (RF) model, represents randomly oriented fibers with the option of having a preferential anisotropy. The second, named Rectangular Duct (RD) model, represents anisotropic layered porous media with channel shapes resembling rectangular ducts surrounded by low permeable sheets of a certain thickness. The effective properties for the two models are presented in Table 1.

2.3 Release of VOC & chemical reactions

Release of VOC from the tobacco material is modeled by first-order Arrhenius reaction kinetics. The kinetic parameters were extracted by multivariate deconvolution techniques and Kissinger's method [10] from thermogravimetric (TG) and Fourier transform infrared spectroscopy (FTIR) experiments by [11], carried out under controlled, low heating rates. As real signals for the release of compounds generally have multiple peaks, several computational compounds, i.e., one computational compound for each peak, were introduced for which the Arrhenius reaction kinetic parameters were extracted. The computational compounds were converted to the respective chemical compounds by a compound transformation matrix.

In addition to the release of VOC from the biomass, char oxidation was modeled according to the method described by [12].

2.4 Aerosol modeling

The aerosol was modeled using a moment approach [13], assuming a log-normal aerosol size distribution with a fixed geometric standard deviation of 1.33. The extended Classical Nucleation Theory (CNT) for multicomponent gas mixtures by [14] was adopted for the nucleation and the models by [7, 15] for aerosol evolution.

3 SIMULATION CASE DESCRIPTION

3.1 Geometry & mesh

The simulation geometry of the EHTS consisted of a Holder, an EHTP, and surrounding air, as shown in Figure 2. The Holder contained an outer shell (OS), battery & electronics (BE), an extractor (EX), a heating element boundary (HEB), and a heater base (HB), whereas the EHTP was built up by a porous tobacco plug (TP), a hollow acetate tube (HAT), a polylactic acid (PLA) filter, paper (PA), a mouth piece filter (FLT), and an outer wall (OW), as shown in Figure 2. The EHTS is in this work represented axi-symmetrically, using a wedge representation, implying that the heating element is represented by a sliver of a pointed cylinder instead of a flat blade. The equivalent diameter of the pointed cylinder was calculated as the average of the diameter equaling the heater surface area and the diameter equaling the volume of the flat heater blade. This choice was made to respect the heat flux as well as the tobacco mass as much as possible, despite the axi-symmetrical representation.

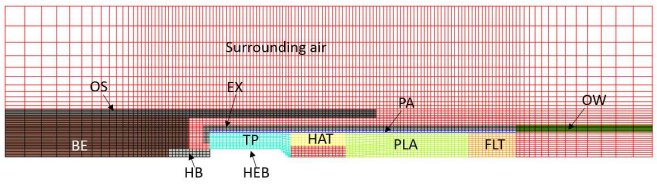

Figure 2: Geometry and mesh.

As a finite volume method was used, the axi-symmetrical 2D computational mesh was represented by a wedge with a single cell layer in the rotational direction around the axi-symmetry axis. The mesh consisted of 4823 hexahedral elements and 118 prism elements in the row closest to the axi-symmetrical axis.

3.2 Simulation conditions

The chemical compounds included in the simulation were: *nitrogen*, *oxygen*, *water*, *carbon monoxide*, *carbon dioxide*, *glycerol*, *nicotine*, and *total aerosol residual*, where the release kinetics for the latter six compounds were considered. The temperature dependent thermophysical properties for the compounds were collected from the databases [16] and [17]. Aerosol mixture properties were computed from mixture laws in [18]. The porous models and the solid thermophysical properties used for each regions are presented in Table 2. As the solid matrix structure is aligned with the principal flow direction in the RD model and ϕ is high in the EHTP regions represented by the RF model, $c_E \approx 0$.

Initially, $\langle T_\alpha\rangle^\alpha = \langle T_\beta\rangle^\beta = 25°\text{C}$, $\langle u_j\rangle = 0$, $\langle p_\alpha\rangle^\alpha = 101325$ Pa, and $N = 0$ m^{-3} in the entire simulation do-

Table 1: Effective properties for RF and RD porous media.

Property	Random fibers (RF)*	Rectangular duct (RD)**
K_{xx}	$wK_{\parallel} + (1-w)K_{\perp}$	$\frac{4ba^3}{3(2a+t^*)(2b+t^*)}\left[1 - \frac{192a}{\pi^5 b}\sum_{n=1,3,\ldots}^{\infty}\frac{1}{n^5}\tanh\frac{n\pi b}{2a}\right]$
$K_{yy} = K_{zz}$	$(1-w)K_{\parallel} + wK_{\perp}$	$\theta^{-1}K_{xx}$
λ^e_{xx}	$w\lambda^{RF}_{\parallel} + (1-w)\lambda^{RF}_{\perp}$	$\phi\lambda_{\alpha} + (1-\phi)\lambda_{\beta}$
$\lambda^e_{yy} = \lambda^e_{zz}$	$(1-w)\lambda^{RF}_{\parallel} + w\lambda^{RF}_{\perp}$	$\frac{1}{2}(\lambda^{RD}_{yy} + \lambda^{RD}_{zz})$
$h_{\alpha\beta}$	$\frac{2\lambda_{\alpha}(3\pi+16(1-\phi))(0.3+0.664Re_{\phi}^{1/2}Pr^{1/3})}{3\pi^2 d}$	$\frac{7.541(1-2.61\gamma+4.97\gamma^2-5.119\gamma^3+2.702\gamma^4+0.548\gamma^5)}{4ab}$
$s_{\alpha\beta}$	$4(1-\phi)/d$	$(a+b)\phi/(ab)$

* The weight w determines the preferential orientation of fibers, d is the fiber diameter. $K_{\parallel}$ and $K_{\perp}$ are taken from [8] and $\lambda^{RF}_{\parallel}$ and $\lambda^{RF}_{\perp}$ from [9] for non-touching parallel cylinders. Re_{ϕ} is the Reynolds number and Pr the Prandtl number.

** a and b are the width and height of a rectangular channel surrounded by a sheet of thickness t^*, calculated from ϕ and $\gamma = b/a$. $\theta = K_{yy}/K_{yy}$ is an anisotropy factor. λ^{RD}_{yy} and λ^{RD}_{zz} are calculated using the approach by [9].

main. The only non-zero initial mass fractions were for oxygen ($Y^{init}_{O_2} = 0.23178$), nitrogen ($Y^{init}_{N_2} = 0.75664$), and water ($Y^{init}_{H_2O} = 0.01158$). For all fields, wedge boundary conditions were applied on the symmetry planes. For p, zero gradient conditions were applied on all boundaries except for the inlets, where the total pressure was specified. A constant velocity 0.1 m/s was set on the right inlet condition to represent ambient flow and zero gradient conditions were specified on all other inlets. No-slip conditions were applied on all solid region boundaries and a Health Canada Intense (HCI) puffing protocol (55 mL, 2 s sinusoidal puffs every 30 s) for 12 puffs was specified on the EHTP outlet, sucking air through the EHTP. Inlet/outlet conditions were specified for the temperature, where flow entering the domain was at 25°C and a zero gradient condition was applied for exiting flow. Between regions, the interface conditions specified by [4] were used. At the surface of the heating element, a uniform and time-varying heater set temperature, as shown in Figure 3, was specified. For Y_k, Z_k, and N, mixed conditions balancing diffusive and convective fluxes were used, whereas zero gradient conditions were applied everywhere else.

The time derivatives of the governing equations were discretized by first-order accurate implicit Euler schemes and the convective terms by the first-order upwind differencing scheme. The Laplacian terms were discretized using linear schemes for smoothly varying variables and tensor harmonic schemes for discontinuous effective properties. Standard OpenFOAM linear solvers were used to solve the equations down to a tolerance 10^{-8} for all equations but the dynamic pressure equation, which was solved to a tolerance of 10^{-10}. Adaptive time stepping was used with a maximum Courant number restriction set to 0.75. The simulation time was 365 s.

4 VALIDATION EXPERIMENTS

To ensure that the simulation results for the temperature distribution and evolution as well as for the delivered chemical compounds are realistic, a set of validation experiments were performed in the EHTP during use.

Temperature measurements: The temperature in the tobacco plug were measured by thermo couples at two locations having different radii for 5 replicates. The thermo couples with tip diameters of 0.25 mm, were inserted into the tobacco plug, by drilling a hole through the Holder and EHTP. The location of the inserted thermo couples were 4.7 mm behind the tip of the heating element (in the direction of the HB) at the radial distances 1.71 mm and 3.4 mm from the blade surface.

Delivery profile measurements: Puff-Per-Puff (PPP) delivery profiles of glycerol and nicotine were measured (5 replicates) during use under a HCI puffing protocol by sampling the EHTP aerosol during individual puffs and directly injecting the sampled aerosol into a gas chromatography (GC) fast scanning quadrupole mass spectrometry (qMS) instrument. As only part of the aerosol was sampled during the puff, the sampled amount of each analyzed compound was rescaled by the amount of that compound found in the Total Particulate Matter (TPM) for all puffs captured on a Cambridge filter.

5 RESULTS & DISCUSSION

To ensure that the simulated tobacco temperature was realistic and representative of the temperature of the tobacco in the EHTP during use, it was compared to thermo couple measurements at two locations in the tobacco plug, as explained in Section 4. As the simulation was performed axi-symmetrically, with the heater represented by a sliver of a pointed cylinder, the representative radial distances from the heater cylinder were calculated (2.55 mm and 3.58 mm from the axi-symmetry axis) to ensure that

Table 2: Region properties.

Region	Type	ϕ	$d/(\mu\text{m})$	w	a_r	$t^*/(\mu\text{m})$	θ	$\rho_\beta/(\text{kg/m}^3)$	$\lambda_\beta/(\text{W/m/K})$	$c_{p,\beta}/(\text{J/kg/K})$
OS, HB	solid	0	–	–	–	–	–	2700	235	900
EX, BE	solid	0	–	–	–	–	–	1320	0.25	1700
PA,OW	solid	0	–	–	–	–	–	804	0.095	830
TP	RD	0.30	–	–	1.0	202.9	10	987	0.159	1374
PLA	RD	0.66	–	–	3.26	50.0	100	1250	0.13	1800
HAT	RF	0.76	19.5	0.43	–	–	–	1280	0.26	1550
FLT	RF	0.85	29.7	0.43	–	–	–	1280	0.26	1550

the amount of tobacco between the thermo couple position in the experiments and the representative point in the simulation geometry were identical for the two experimental positions. As shown in Figure 3, the simulated temperatures were within the experimental range indicated by the gray areas at both positions. The good fits indicate that the heat conduction and heat loss in the EHTS were well captured in the simulation. It can also be seen that despite the good fit of the temperature levels, the drops in the experimentally measured temperatures during puffs were not well captured in the simulation. This may indicate that the interfacial heat transfer coefficient (based on constant temperature at fully developed flow conditions) was too low in the simulation, as this assumption is questionable during puffs. Moreover, the experimentally measured temperature is not purely the tobacco temperature, but a mix between the tobacco and the gas temperature, whereas in the simulation it is purely the tobacco temperature. Nevertheless, the general trend of the tobacco temperature was well captured by the simulation and was well below the set temperature of the heating blade (T_{hst}).

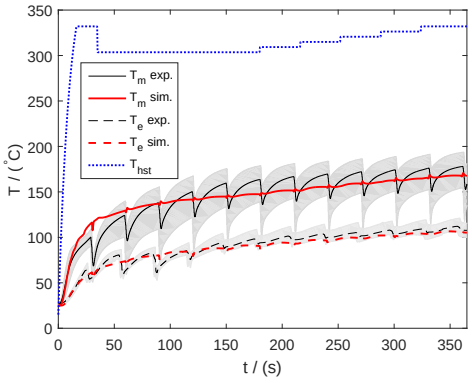

Figure 3: Temperature evolution compared to experimental data at two locations in the TP and the heater set temperature (T_{hst}).

As shown in Figure 4, the VOC delivery profiles of the experiments were well captured in the simulation for both glycerol and nicotine, even though small over-predictions can be seen in puffs 3, 4 and 7 for glycerol and slight under-predictions can be seen for the simulated nicotine delivery in puffs 4-10.

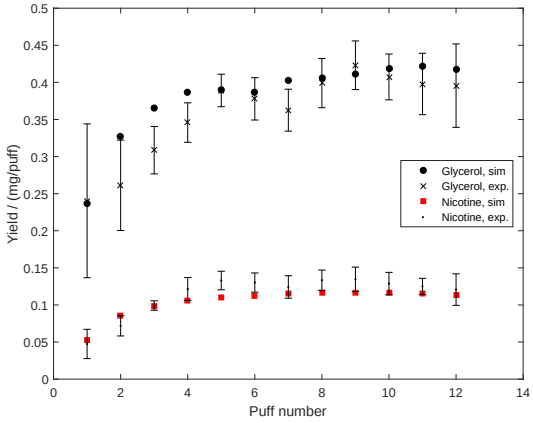

Figure 4: Puff-per-puff yields compared to experimental data.

The solid tobacco temperature isotherms in the tobacco plug right before puffs 3 & 6 (Figure 5a) and 9 & 12 (Figure 5b), indicate that the temperature of the tobacco was below the heater set temperature. As also shown in Figure 5a and 5b, the isotherms were slowly moving in the positive radial direction with increasing time. This advancing temperature gradient resulted in a continuous release of VOC from fresh portions of tobacco during use, as shown in Figure 4.

As shown in Figures 5, most of the tobacco plug was kept at low temperature throughout the HCI puffing protocol. To visualize this further, the volume fractions of the plug having temperatures at certain ranges are shown in Figure 6 for all time instances during the HCI protocol. Less than 4.2% of the plug volume was shown to be ≥ 300°C (but ≤ 350°C), whereas more than 74.7% of the plug volume was ≤ 200°C during the entire puffing protocol. The cooling down of the tobacco temperature during puffs is clearly shown by the peaks in Figure 6.

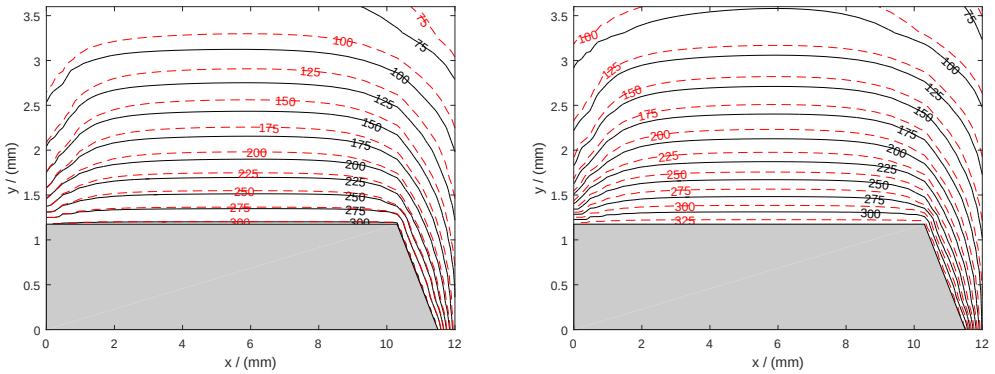

(a) Puffs 3 & 6 (b) Puffs 9 & 12

Figure 5: Temperature isotherms in the tobacco plug for the time instants: $t = 90$s (before 3$^{\text{rd}}$ puff) (black solid lines) and $t = 180$s (before 6$^{\text{rd}}$ puff) (red dash-dot lines).

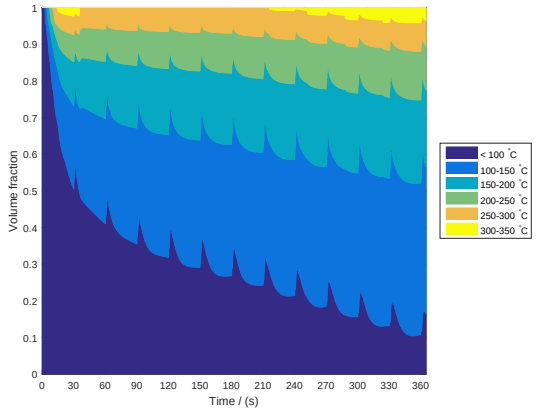

Figure 6: Volume fraction of tobacco plug within certain temperature ranges.

6 CONCLUSIONS

Transient and density varying flow, heat and mass transfer in an EHTP containing an anisotropic porous biomass plug was simulated. The simulation results agreed well with experimental data of the temperature in the biomass plug and the delivery profiles of glycerol and nicotine during use under a HCI puffing protocol. It was shown that the temperature of the tobacco plug remained below the heater set temperature at all times during use and less than 4.2% of the plug volume was ≥ 300°C (but ≤ 350°C) at any time. More than 74.7% of the tobacco was ≤ 200°C during the entire puffing protocol. The close match between numerical and experimental results indicates that most relevant physical and chemical processes were accounted for in the presented, geometrically simplified, numerical model.

ACKNOWLEDGEMENTS

All authors are employed by Philip Morris Products S.A. (part of Philip Morris International group of companies), which is the sole source of funding and sponsor of this research. Thanks to PMI R&D laboratories for providing experimental data and to Dr. C. Winkelmann for model development.

REFERENCES

[1] S. Whitaker, editor. *The Method of Volume Averaging*. Kluwer Academic Publishers, Dordrecht, 1999.

[2] C.T. DeGroot and A.G. Straatman. *J. Heat Transfer*, 134(4):042603–042603, 02 2012.

[3] C.T. Hsu. *ASME. J. Heat Transfer*, 121(3):733–739, 1999.

[4] L. Betchen et al. *Numer. Heat Transfer, Part A*, 49(6):543–565, 2006.

[5] C.T. DeGroot et al. *Numer. Heat Transfer, Part B*, 60(4):252–277, 2011.

[6] M. Nordlund et al. *J. Comput. Phys.*, 306:199 – 215, 2016.

[7] E.M.A. Frederix et al. *Int. J. Multiphase Flow*, 74:184–194, 2015.

[8] B.R. Gebart. *J. Compos. Mater.*, 26(8):1100–1133, 1992.

[9] C.T. Hsu et al. *ASME. J. Heat Transfer*, 117(2):264–269, 1995.

[10] H. E. Kissinger. *J. Res. Nat. Bur. Stand.*, 57(4):217–221, 1956.

[11] F. Barontini et al. *Ind. Eng. Chem. Res.*, 52(42):14984–14997, 2013.

[12] M. Muramatsu and S. Umemura. *Beiträge zur Tabakforschung / Contributions to Tobacco Research*, 11(2):79Ũ86, 1981.

[13] H.C. Hinds. *Aerosol Technology: Properties, Behavior, and Measurement of Airborne Particles*. John Wiley & Sons Inc., New York, 2nd edition, 1999.

[14] M. Nordlund and A. K. Kuczaj. *Int. J. Chem., Mol., Nucl., Mater. Metall. Eng.*, 10(4):326 – 338, 2016.

[15] C. Winkelmann et al. *Int. J. Numer. Methods Fluids*, 74 (5):313–334, 2014.

[16] VDI-Gesellschaft Verfahrenstechnik und Chemieingenieurwesen and VDI Gesellschaft. *VDI Heat Atlas*. Springer, 2010.

[17] CAMEO Chemicals database. `http://cameochemicals.noaa.gov`. 2015.

[18] B.E. Pauling et al. *The Properties of Gases and Liquids*. McFraw-Hill, New York, 2001.